Enhancement of Ultrasound Microbubble and Blood Flow Imaging using Similarity Measurement

Chengwu Huang, *Member, IEEE*, U-Wai Lok, *Member, IEEE*, Jingke Zhang, *Member, IEEE*, Ping Gong, *Member, IEEE*, Kate M. Knoll, Kathryn A. Robinson, Andrew J. Bentall, and Shigao Chen, *Senior Member, IEEE*

***Abstract*—Recent advancements in ultrasound technologies, such as ultrasound localization microscopy and ultrafast ultrasound Doppler, have enabled high-definition imaging of microvasculature. However, detecting weak microbubble or blood flow signals amid strong background noise remains a challenge, particularly in deep tissues. This study aims to enhance the signal contrast of microbubble and blood flow by leveraging their distinct spatial-temporal coherence in comparison to undesired noise for robust microbubble detection and microvascular imaging. We propose to quantify the signal coherence based on similarity analysis of beamformed ultrasound microbubble/blood flow data within the plane wave imaging framework. A spatial pixel is considered more likely to be a true microbubble/blood flow signal with a higher level of similarity, which can be measured by either of the following methods: 1) spatially block-wise normalized cross-correlation between two compounded frames; 2) temporally normalized autocorrelation across multiple compounded frames; 3) normalized cross-correlation between two subsets of post-compounded frames; 4) normalized autocorrelation of the pre-compounded data across angular direction. The original microbubble/blood flow signal is then weighted by the similarity measurement on a pixel-by-pixel basis to generate images with an improved signal contrast. The robustness of the proposed methods was first demonstrated in both phantom experiments and *in vivo* microbubble data from kidney transplant. We further validated their feasibility in blood flow imaging without the use of microbubbles based on *in vivo* data of human liver and kidney. Significant contrast improvement was observed, facilitating better visualization and detection of both microbubble and noncontrast microflow signals, which indicates a great potential of the methods for improved microvascular imaging and widespread clinical translation.**

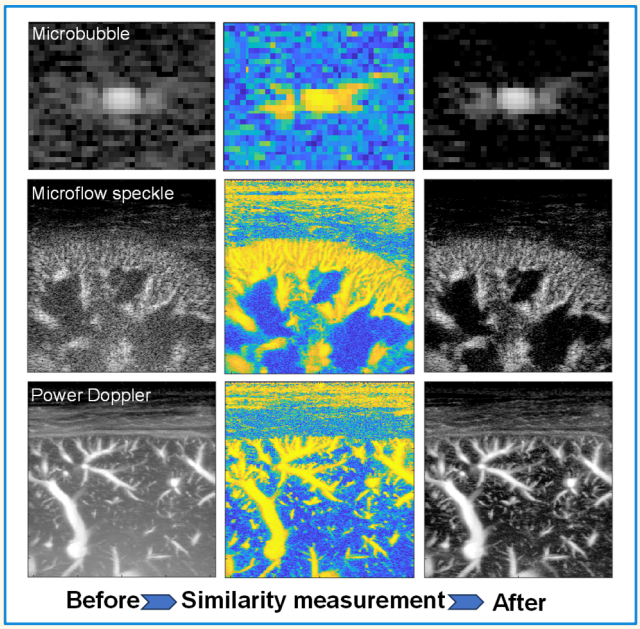

***Index Terms*—Blood flow, Coherence, Microbubble, Ultrasound localization microscopy, Ultrasound Doppler**

I. Introduction

Contrast-enhanced ultrasound (CEUS) and Doppler ultrasound are common clinical ultrasound modalities broadly used to provide valuable insights into tissue perfusion and blood flow hemodynamics [1, 2]. These modalities operate by transmitting ultrasound pulses into target tissues, capturing and isolating backscattering echo signals from either ultrasound contrast agents (*e.g.*, microbubbles) or moving red blood cells to form blood flow images. Ultrasound microbubbles are gas-filled microspheres with a size of several μm and are routinely used as contrast agents administered into the bloodstream via intravenous injection to provide strong ultrasound

This work was partially supported by the National Institutes of Health under award number R01DK129205, R01EY035084 and R21AR076028. The content is solely the responsibility of the authors and does not necessarily represent the official views of the National Institutes of Health. The Mayo Clinic and some of the authors (C. H., J. Z., and S.C.) have a potential financial interest related to the technology referenced in this research. (*Corresponding author: Shigao Chen*)

Chengwu Huang, U-Wai Lok, Jingke Zhang, Ping Gong, Kate M. Knoll, Kathryn A. Robinson and Shigao Chen are with the Department of Radiology, Mayo Clinic College of Medicine and Science, Rochester, MN 55905, USA (e-mail: Huang.Chengwu@mayo.edu; Lok.U-Wai@mayo.edu; Zhang.Jingke@mayo.edu; Gong.Ping@mayo.edu; Knoll.Kate@mayo.edu; Robinson.Kathryn1@mayo.edu; Chen.Shigao@mayo.edu).

Andrew J. Bentall is with the Division of Nephrology and Hypertension, Mayo Clinic, Rochester, MN 55905, USA (e-mail: Bentall.Andrew@mayo.edu).

Highlights

- **Several methods to effectively enhance the contrast of microbubble and blood flow signals in ultrasound imaging were proposed by leveraging the spatial-temporal coherence of the ultrasound beamformed data.**
- **The proposed methods were demonstrated feasible in phantom and *in vivo* studies, showing substantial contrast improvement in microbubble, microflow speckle and power Doppler imaging.**
- **The robustness and easy implementation of the methods may enable widespread integration into techniques like ultrasound localization microscopy and ultrafast ultrasound Doppler to facilitate better microvascular imaging.**

backscattering from the blood flow [3, 4]. Localizing and tracking the individual microbubbles in the bloodstream via high frame rate ultrasound has fostered the recent advancement of super-resolution ultrasound microvessel imaging, known as ultrasound localization microscopy (ULM) [5-7]. ULM identifies individual microbubbles and utilizes the center position of microbubbles to reconstruct the microvascular image with a spatial resolution beyond ultrasound diffraction limit [5-7]. Maintaining a favorable microbubble signal-to-noise ratio (SNR) or contrast-to-noise ratio (CNR) is thus critical for accurate microbubble detection, localization, and the subsequent high-quality microvascular imaging [5, 7]. The use of unfocused ultrasound transmission (e.g., plane wave imaging) in the state-of-the-art ULM settings may lead to relatively low SNR in deep tissue, posing challenges in clinical scanning scenarios. In such cases, low SNR/CNR can result in inaccurate and false microbubble detections that eventually compromises microvascular imaging. Therefore, methods to improve the detection of individual microbubble are highly warranted for robust microbubble localization and imaging, especially for challenging clinical scenarios.

In the realm of Doppler ultrasound without contrast agents, the echo reflections from the red blood cells are substantially lower [8]. Consequently, imaging of the weak flow signal from the microvasculature poses an even greater challenge. Conventional Doppler ultrasound involves the repetitive transmission and reception of ultrasound pulses in target tissues at a high pulse repetition frequency (PRF), with a typically low number of repetitions (e.g., 8 to 32, denoted as packet size or ensemble size in Doppler ultrasound) [1, 9]. A clutter filter or wall filter is applied to the received data packet to eliminate tissue clutter from the blood flow signals by leveraging the temporal frequency difference among signal components [1, 9]. Subsequently, blood flow images, such as color Doppler and power Doppler images, are derived from the extracted blood flow signals. For instance, a power Doppler image can be generated from one packet of flow data by accumulating or averaging the power of the blood flow signal over the temporal dimension (e.g., slow time dimension) [1]. The sensitivity of Doppler ultrasound in detecting small vessels can be highly increased by employing a prolonged data acquisition *i.e.*, a larger packet size [8, 10, 11]. The introduction of ultrafast ultrasound imaging and advanced spatial-temporal clutter filters like the singular value decomposition (SVD) filter, has further marked a leap in Doppler sensitivity over the past decade, enabling ultrasound imaging of microvascular without the need of contrast agents [8-10]. In contrast to accumulating blood flow signals over a large packet size to generate one power Doppler image, an alternative approach involves displaying single frames of blood flow speckle pattern without accumulation in a way similar to b-flow imaging [12-14]. This approach enables a direct and dynamic visualization of ultrasound speckle variations of blood flow with high temporal resolution [12-14]. In this scenario, the SNR/CNR of the single-frame blood flow signals becomes pivotal, especially for weak microflow signal.

Despite the advancements, improving the detection and visualization of microbubble and weak blood flow signal in small vessels remains an ongoing pursuit. Instead of taking the zero-lag autocorrelation as an estimation of the power Doppler, non-zero lag autocorrelation along temporal dimension has proven beneficial for the detection of weak microbubbles, particularly for slow-moving microbubbles which pose higher temporally coherence [15]. The temporal fluctuation of the microbubble signals was further elaborated via high-order statistics calculation to achieve both spatial resolution improvement and background noise suppression [16]. A nonlinear compounding process that leverages the autocorrelation over angular dimension of the multi-angle plane wave imaging has also shown promise in improved microvascular imaging without the need for contrast agents [17, 18]. Notably, by spitting the channel data before beamforming or the pre-compounding plane wave angle data into two nonoverlapping subsets and calculating the cross-correlation between subsets of data can substantially improve the noise suppression in blood flow image [18-20]. The underlying principle shared by these methods is that the undesired components (noise or artifacts) can be suppressed due to their uncorrelated nature among data, while target signal (microbubble or blood flow) exhibits higher coherence, either spatially or temporally, and thus be enhanced during the auto- or cross-correlation calculations. Additional approaches include estimating the noise floor of power Doppler image and applying noise floor equalization or subtraction for effective noise debiasing [21-23]. Above methods, however, are primarily tailored for improving the final power Doppler or blood flow images generated from a packet of data with a relatively large packet size (e.g., > 100 ensembles), which may not be directly applied to single frame of microbubble and blood flow signals. Coded excitation or nonlinear imaging strategies provide an alternative to improve SNR for both microbubble and blood flow signals on a single frame basis [24-26]. But these methods may require proper encoding-decoding procedures and increased ultrasound transmissions. In terms of signal processing, noise compensation is achievable during the process of SVD clutter filtering by removing higher-order singular components [27, 28]. However, a proper cut-off selection to separate noise and blood flow will be required,

which may not be as effective when blood flow signal and noise are not well separatable in the singular value domain [28]. More advanced clutter filters such as high-order SVD and Cauchy-RPCA filters exhibit promise while they are still relatively computationally expensive [29-32]. The spatial coherence of ultrasound backscattering in the channel domain has also been well established and leveraged to produce coherent flow power Doppler image with superior flow detection, and effective suppression of noise and incoherent reverberation clutter [33, 34]. In addition to spatial coherence among channels of data, further exploration of the angular coherence theory has also provided a deep insight into signal coherence among different transmit angles [35]. This has resulted in significant image quality improvement in both B-mode ultrasound and blood flow images through beamformed data in multi-angle plane wave imaging [35, 36]. More recently, the spatial coherence or a combination of spatial and angular coherence of the blood flow signal after SVD filtering in the channel domain, is leveraged to generate a pixel-wise coherence factor weighting map, which can be applied back to the blood flow signal to produce power Doppler image with substantial contrast improvement [37, 38]. While channel data can offer a higher flexibility for signal handlings and denoising operations, these channel domain approaches are in general computationally intensive due to the significantly larger amount of channel data to be processed [35, 37, 38].

In this study, we will introduce several methods dedicated to enhancing the signal contrast in both microbubble and blood flow imaging specifically based on the beamformed ultrasound data within the ultrafast plane wave imaging framework. As microbubble or blood flow signal are assumed to be distinct from the undesired noise in terms of spatial-temporal coherent patterns, the pixels of signal and pixels of noise in an image can thus be differentiated based on their levels of signal coherence. We propose to quantify the signal coherence by measuring the similarity of signal along either temporal, spatial, angular dimensions, or a combination thereof based on the beamformed data before or after spatial plane wave imaging compounding. The resulting similarity measurements are subsequently used as weighting maps applied back to the microbubble or blood flow signal to achieve signal enhancements for each individual ultrasound frame. We will first elaborate the methods in the context of microbubble imaging, which will facilitate better microbubble detection for contrast-enhanced microvascular imaging and future ULM applications. We then extend the application of these methods to blood flow imaging without using contrast agents, with specific focus on enhancing the weak flow signal of small vessels on single-frame speckle images, as well as power Doppler images that are accumulated from a packet of data.

II. Materials and Methods

A. Principle of signal enhancement methods

In this study, we aim to enhance microbubble detection and blood flow imaging by leveraging the beamformed In-phase and Quadrature (IQ) data before or after spatial compounding within ultrafast plane wave imaging framework, as schematically illustrated in Fig. 1. It is assumed that the characteristics of target signals (microbubble or blood flow) and undesired background noise are distinct in terms of spatial and/or temporal variations. The undesired noise exhibits high spatial or temporal variations, *i.e.*, the pixel of noise varies in terms of pixel intensity and phase across different ultrasound

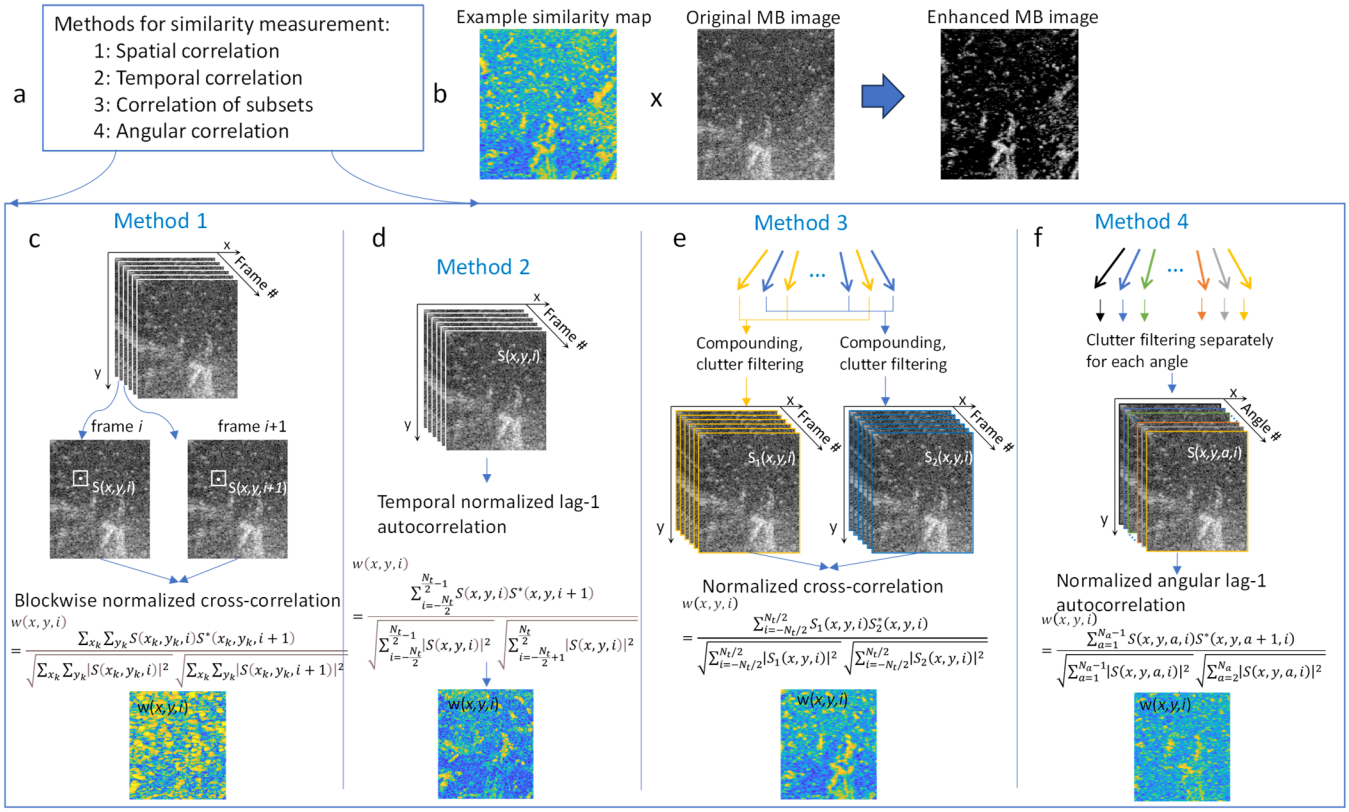

Fig. 1. Schematic diagram of the similarity-based signal enhancement methods to improve microbubble and blood flow imaging.

transmissions and receptions. However, the true target signals are less varying and more coherent, *i.e.*, the pixel of true target signal tends to be more similar in terms of signal intensity and phase across ultrasound transmission/reception events. The signal coherence or similarity levels of the tissue clutter filtered data can therefore be estimated to distinguish between true target signals and undesired background noise.

In this study, four distinct similarity measurement methods that leverage spatial and/or temporal coherence of the pre- or post-compounding plane wave imaging data are proposed to enhance the image contrast of target signals, as elaborated below. With similarity measurement, pixels of high similarity are considered real targets and can be enhanced, while those with poor similarity are identified as undesired noise and are suppressed. This selective enhancement and suppression process can thus result in an improved contrast of the target signal in comparison to the background. Specifically, the similarity map estimated from each method is applied as a weighting map to the original noise-contaminated data on a pixel-by-pixel basis to achieve signal enhancement, as illustrated in Fig. 1b.

1) Method 1: Block-wise normalized spatial cross-correlation between two adjacent ultrasound frames

This method is directly based on the ultrasound data after plane wave compounding and tissue clutter filtering. The given ultrasound data are assumed to contain majorly target signals (microbubble or blood flow signal) and undesired background noise. The similarity of the ultrasound signal is estimated as a block-wise normalized cross-correlation between two adjacent ultrasound frames, as example shown in Fig. 1c. Specifically, the intensity of each pixel in the similarity map represents the normalized cross-correlation coefficient calculated between small signal blocks of the two ultrasound frames at the corresponding position of that pixel (Fig. 1c), as:

$$w(x,y,i) = \frac{\sum_{x_k}\sum_{y_k} S(x_k,y_k,i)S^*(x_k,y_k,\ i+1)}{\sqrt{\sum_{x_k}\sum_{y_k}|S(x_k,y_k,i)|^2}\sqrt{\sum_{x_k}\sum_{y_k}|S(x_k,y_k,i+1)|^2}} \quad (1)$$

where $S(x,y,i)$ is the post-compounded ultrasound data of the microbubble, with x, y corresponding to the axial, lateral coordinates (spatial dimensions) and i corresponding to post-compounded frame number (temporal dimension). Here $\sum_{x_k}\sum_{y_k} S$ indicates the summation across the small spatial block center at (x, y). In this study, a fixed block size of 5×5 pixels will be used throughout the study. $|S|$ indicates the absolute value and * represents complex conjugation. It is assumed that the movement of microbubble is small at a high imaging frame rate setting, and thus spatial feature is similar (highly correlated) between two frames. In contrast, the noise block between two frames is considered random and uncorrelated. Therefore, the correlation map according to Eqn. 1 (Fig. 1c) represents a map of similarity that provides information on the likelihood of a pixel being the true target or noise. Based on this assumption, pixels in the original ultrasound image with a high similarity level (*i.e.*, high normalized cross-correlation coefficient) can be enhanced while pixels with a low similarity level (*i.e.*, low normalized cross-correlation coefficient) can be suppressed. As illustrated in Fig. 1b, the similarity map is directly used as a weighting map applied back to the microbubble image to achieve signal enhancement, *i.e.*, $S_e(x,y,i) = S(x,y,i)\cdot w(x,y,i)$.

2) Method 2: Normalized temporal autocorrelation across multiple ultrasound frames

This section introduces a temporal autocorrelation method employing multiple post-compounded ultrasound frames, as depicted in Fig. 1d. In contrast to existing literature that utilizes non-normalized autocorrelation coefficient as the blood flow image [15], here we propose using normalized autocorrelation of the temporal signal to generate a similarity-based weighting map, and then apply this map back to the ultrasound frames to achieve microbubble signal enhancement. Again, assume $S(x,y,i)$ represents the post-compounded multi-frame ultrasound data of the microbubble or blood flow contaminated with noise, where x and y correspond to the spatial dimensions, and i is the frame number corresponding to the temporal dimension (Fig. 1d). At a pixel location (x, y), the level of similarity can be calculated as a normalized autocorrelation of $S(x,y,i)$ along temporal direction with a specific lag. In this study, we calculated the normalized lag-one autocorrelation, which is the normalized correlation of $S(x,y,i)$ with a temporally lag-one version of itself, *i.e.*, $S(x,y,i+1)$, as:

$$w(x,y,i) = \frac{\sum_{i=-\frac{N_t}{2}}^{\frac{N_t}{2}-1} S(x,y,i)S^*(x,y,\ i+1)}{\sqrt{\sum_{i=-\frac{N_t}{2}}^{\frac{N_t}{2}-1}|S(x,y,i)|^2}\sqrt{\sum_{i=-\frac{N_t}{2}+1}^{\frac{N_t}{2}}|S(x,y,\ i)|^2}} \quad (2)$$

where N_t is the number of post-compounded temporal frames involved in the calculation of similarity map. A larger N_t can thus result in smoother and better similarity measurement, while a smaller N_t offers a higher temporal resolution of similarity estimation. In this study, a consistent $N_t = 50$ is used throughout the study. While a higher lag of autocorrelation may be used, choosing a lag of one frame can typically maximize the temporal coherence of the microbubble signal, and better facilitate the discrimination of microbubble and noise.

3) Method 3: Normalized cross-correlation between two subsets of post-compounded frames

The method described here involves separation of the plane wave angle data into two subgroups to perform spatial compounding and tissue clutter filtering separately, and then measurement of similarity based on the normalized cross-correlation of the two subsets, as illustrated in Fig. 1e. In ultrasound plane wave imaging where multiple unfocused waves are transmitted sequentially at different steering angles, the received data corresponding to different transmitting angles are split into two subgroups and coherently added separately to generate two series of post-compounded frames, similar to the method described in a previous study [20]. With such data formation settings, the level of signal similarity is estimated by a normalized cross-correlation between the two data subsets across multiple temporal frames for each spatial pixel. Specifically, assuming $S_1(x,y,i)$ and $S_2(x,y,i)$ represent the two data subsets of the target signal contaminated with noise, where x and y corresponding to the spatial dimensions, and i is the frame number in temporal dimension (Fig. 1e), the degree of similarity is calculated as:

$$w(x,y,i) = \frac{\sum_{i=-N_t/2}^{N_t/2} S_1(x,y,i)S_2^*(x,y,i)}{\sqrt{\sum_{i=-N_t/2}^{N_t/2}|S_1(x,y,i)|^2}\sqrt{\sum_{i=-N_t/2}^{N_t/2}|S_2(x,y,i)|^2}} \quad (3)$$

Where N_t is the number of post-compounded frames involved in each subset. A larger N_t implies the use of more temporal frames and thus an improved smoothness of similarity map, while smaller N_t is associated with a higher temporal resolution for the similarity map calculation. To be consistent, we will use a fix $N_t = 50$ throughout the study. While the way in which the plane wave angle data is separated into two subgroups can be arbitrary, here we choose the odd numbers of angular data as one subgroup and even numbers of angular data as a second subgroup and perform compounding separately. In this way, both spatial and temporal differences of the two compounded subsets are considered minimize, and thus maximizing the coherence of the microbubble signal for optimal differentiation of the target signal and noise.

4) Method 4: Normalized autocorrelation across angular direction

In this method, we leverage the angular coherence of microbubble or blood flow signal in multi-angle plane wave imaging. For each ultrasound transmission at a specific steering angle, the received data is used to beamform an angular frame corresponding to this transmitting angle before spatial compounding. We apply clutter filtering to the pre-compounded data corresponding to each transmitting angle and then assess the signal variation across the angular direction. The similarity measurement is obtained as the normalized lag-one autocorrelation of the data along the angular direction, as illustrated in Fig. 1f. Assume $S(x,y,a,i)$ is the given pre-compounded ultrasound data of the microbubble or blood flow signal contaminated with noise, where x and y corresponding to the spatial dimensions, a is the number of plane wave angles corresponding to the angular direction, and i is the frame number corresponding to the temporal dimension (Fig. 1f). At a given pixel location (x, y) of temporal frame i, the degree of similarity can be calculated as:

$$w(x,y,i) = \frac{\sum_{a=1}^{N_a-1} S(x,y,a,\,i)S^*(x,y,a+1,\,i)}{\sqrt{\sum_{a=1}^{N_a-1}|S(x,y,a,\,i)|^2}\sqrt{\sum_{a=2}^{N_a}|S(x,y,a,\,i)|^2}} \quad (4)$$

Where N_a is the number of steering angles in multi-angle plane wave imaging setting. This similarity map will then be applied to the spatial compounded data on a pixel-by-pixel basis as a weighting map to achieve signal enhancement (Fig. 1b).

B. In the context of noncontrast microvessel imaging

A power Doppler image in Doppler ultrasound is typically generated from accumulation of signal power across a packet of ultrasound frames after tissue clutter filtering [1], as depicted in Fig. 2. The intensity of the power Doppler is considered proportional to the fractional moving blood volume, offering a clinically relevant perfusion quantification [39]. Alternatively, b-flow imaging provides an additional method for blood flow visualization, which extracts the blood flow signal and displays the ultrasound speckle pattern of moving blood at high frame rate [12-14]. The elevated sensitivity of blood flow detection enabled by the state-of-the-art clutter filtering techniques and ultrafast imaging is now making it possible to visualize the backscattering speckle pattern of the slow blood flow from small vessels. In this study, in addition to the generation of microvascular power Doppler image (Fig. 2d), we will also display the tissue clutter filtered data frame by frame to visualize the flow speckle pattern of the microvascular, hereafter referred to as microflow speckle imaging, as illustrated in Fig. 2c. This highly sensitive imaging of the blood flow speckle at high frame rate can provide an intuitive representation of flow dynamics that may not be attainable through power Doppler alone and may be of relevant for specific clinical applications [13, 14]. However, the persistent challenge of low SNR and CNR in individual ultrasound frames remains a major hurdle for such a microflow speckle imaging mode. The similarity measurements proposed above can therefore be applied to the specking imaging on a single-frame basis, with high potential to improve the discernibility of the microflow in small vessels. Simultaneously, the enhanced power Doppler image will also be obtained from the power accumulation of the enhanced flow signal. The feasibility of the proposed techniques for signal enhancement in both microflow speckle imaging and microvessel power Doppler imaging without the use of contrast agents will be evaluated *in vivo* in this study.

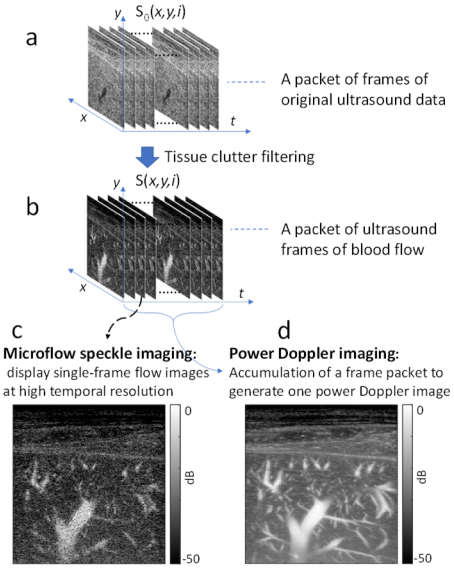

Fig. 2. Schematic illustration of ultrasound microflow speckle imaging and microvascular power Doppler imaging.

C. Experimental studies

1) Vessel phantom study

A phantom experiment was performed using a custom-designed flow channel phantom (Gammex Inc., Middleton, WI, USA) with a 2-mm inner diameter straight flow channel. The outlet of the channel was connected to a syringe pump (Model NE-1010, New Era Pump Systems Inc., Farmingdale, NY, USA), which allowed pumping of the microbubble suspension through the flow channel at a constant flow rate. The Definity microbubble (Lantheus medical imaging, Billerica, MA, USA) suspension was sufficiently diluted to ensure the sparsity of microbubbles and allow isolated individual microbubbles passing through the flow channel during data acquisition. This

intentional setup allowed a focused evaluation of the proposed methods on individual microbubble signals. A Verasonics Vantage ultrasound system (Verasonics Inc., Kirkland, WA, USA) equipped with a GE 9L linear array transducer (GE Healthcare, Wauwatosa, WI, USA) was utilized. A 10-angle plane wave imaging was implemented with an angle increment of 1° between successive transmission and a PRF of 10 kHz. The center frequency of transmitted ultrasound was 6.25 MHz, with a transmitted pulse length of 1 cycle. The beamformed IQ data corresponding to each transmitted angle before spatial compounding were captured and stored for subsequent post-processing. The spatial pixel resolution of the beamformed IQ data was 0.5λ in both axial and lateral dimensions, where λ = 0.246 mm representing the wavelength. Spatial compounding was performed offline, and the frame rate of the compounded data was set to be 500 Hz. A packet of IQ data, corresponding to 400 post-compounded frames (0.8 s), was captured in each acquisition. A deliberately low transmit voltage of 2 V (one-side voltage) was used to emulate a low SNR and CNR condition.

2) *In vivo kidney transplant study*

The *in vivo* study was approved by the Institutional Review Board (IRB) of Mayo Clinic, and Written informed consent was obtained from each patient. A clinical Resona 7 ultrasound scanner (Shenzhen Mindray Bio-Medical Electronics Co. Ltd, Shenzhen, China), equipped with an L9-3U linear array transducer was used for ultrasound scanning and data acquisition from the 40-year-old kidney transplant patient. A 6-angle plane wave imaging, with transmitting angle spanning from −10° to 10° and a transmitted frequency of 3.6 MHz (1.5 cycles of pulse length, PRF = 2.1 kHz) was implemented. The frame rate of the post-compounded data was 346 Hz, and a mechanical index (MI) of 0.2 was used for the plane wave imaging. The beamformed ultrasound IQ data corresponding to each transmitted angle before spatial compounding were acquired after the administration of a bolus of 2.4 ml Lumason microbubble (Bracco Diagnostics Inc., Monroe Township, NJ, USA) followed by a saline flush through intravenous injection. The spatial resolution of the beamformed IQ data was 0.095 mm in axial direction and 0.23 mm in lateral direction. Ultrasound imaging was focused on the long-axis view of the transplanted kidney with patient in a supine position. The patient was instructed to hold their breath for less than 10 seconds during each data acquisition session. A packet of beamformed IQ data captured from this patient, corresponding to 500 post-compounded frames (1.45 s), was utilized to the evaluation of the methods proposed in this study.

3) *Noncontrast in vivo study in human liver and kidney*

The study was approved by the Institutional Review Board (IRB) of Mayo Clinic, and written informed consent was obtained from the participant. The plane wave ultrasound data of a human liver and kidney without using ultrasound contrast agents were captured from a healthy volunteer. The same Verasonics Vantage ultrasound system (Verasonics Inc., Kirkland, WA, USA) and the GE 9L linear array transducer (GE Healthcare, Wauwatosa, WI, USA) was utilized. The imaging parameters were the same as those in the phantom study, except for a transmit voltage of 50 V (one-side voltage) was used for the noncontrast *in vivo* data acquisition. Beamformed IQ data of the 10-angle plane wave imaging were captured before spatial compounding. The offline spatial compounding of the saved data in each acquisition will yield a stack of 400 post-compounded ultrasound frames (0.8 s) at a frame rate of 500 Hz. The volunteer was instructed to hold the breath during each data acquisition session to minimize breathing tissue motion.

D. Data processing

Spatial compounding is performed offline to generate the post-compounded data, followed by SVD clutter filtering applied to the compounded data to suppress tissue clutters. Assume the compounded data $S_0(x, y, i)$ has a size of $N_x \times N_y \times N_t$, where N_x and N_y represent data size in axial and lateral dimensions, and N_t is the number of compounded frames corresponding to temporal dimension. This original data is first reshaped into a 2D Casorati matrix with a dimension of $N_x N_y \times N_t$, where each column represents a vectorized frame. The SVD of the 2D Casorati matrix is then computed, followed by a singular value thresholding process to eliminate the tissue clutter associated with low-order, larger singular values. More specifically, a 'turning point' of singular value curve is identified for each dataset as the threshold and the singular values exceeding this threshold are set to zero. Subsequently, an inverse SVD calculation is performed to reconstruct the microbubble data in the case of contrast-enhanced imaging or the blood flow data for noncontrast imaging. The clutter-filtered 2D Casorati matrix is then reshaped back to the original spatial-temporal dimension $N_x \times N_y \times N_t$, as $S(x, y, i)$. The similarity map obtained based on the proposed methods is utilized to weigh the clutter-filtered microbubble or blood flow data $S(x, y, i)$, yielding an enhanced imaging for each frame individual frame, as illustrated in Fig. 1b. Additionally, a power Doppler image can also be obtained by the accumulation of the signal power along temporal direction, as indicated in Fig. 2d. The detailed methods of the similarity measurement are elucidated in Fig. 1c-1f. In methods 1 and 2, only the post-compounded data is required, and the similarity map is generated by either the spatial correlation of adjacent compounded frames or the temporal autocorrelation across multiple compound frames. In method 3, the data corresponding to different transmitting angles are split into two interleaving subsets for spatial compounding to generate two subsets of data separately. The same SVD clutter filtering is applied to each data subset to extract microbubble or blood flow data for subsequent similarity measurement (Fig. 1e). For method 4, the data corresponding to each transmitting angle is considered a data subset and the SVD filtering is applied to each subset to remove tissue clutter. The similarity measurement is then performed by leveraging the angular coherence of signal across transmitting angle direction, as indicated in Fig. 1f.

III. Results

A. Microbubble data in vessel phantom

The B-mode image of flow vessel phantom is presented in Fig. 3a, and a frame microbubble image derived from SVD-based clutter filtering is displayed in Fig. 3b (see supplemental video for a stack of microbubble frames). The utilization of a very sparse microbubble concentration enables the clear

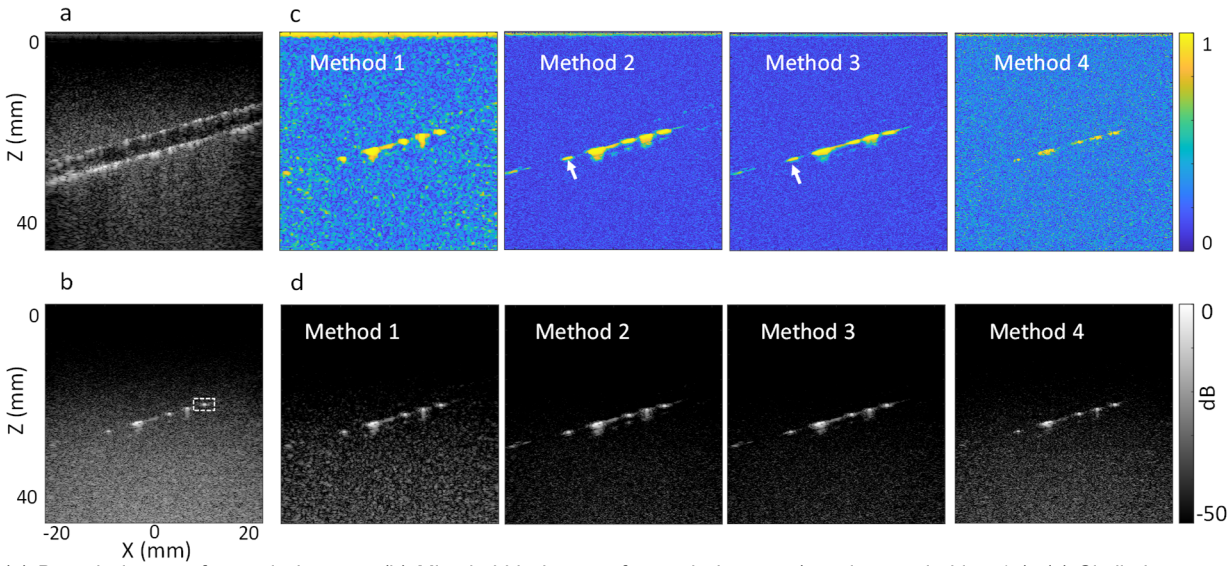

Fig. 3. (a) B-mode image of vessel phantom. (b) Microbubble image of vessel phantom (supplemental video 1a). (c) Similarity maps for this microbubble image obtained using four different methods. (d) Corresponding enhanced microbubble images based on weighting using the four methods (supplemental videos 1b-1e).

imaging of spatially isolated microbubbles within the flow channel, albeit contaminated with a high level of background noise (Fig. 3b). The corresponding similarity maps for this frame are depicted in Fig. 3c using each of the four proposed methods. These maps provide crucial information on facilitating the identification of the microbubbles, where a higher value in the map corresponds to a higher possibility of the pixel being a true microbubble signal. Figure 3d showcases the microbubble images obtained by weighting the original image (Fig. 3b) with the corresponding similarity maps (Fig. 3c), resulting in a substantial improvement of signal contrast (see supplemental videos 1b-1e). To highlight a single microbubble in the image, Fig. 4a zooms in on the region indicated by the rectangle in Fig. 3b. The lateral profile of this microbubble is illustrated in Fig. 4b, and the average of the profile segments in the background region (segments beyond the main and side lobes, indicated by the arrows in Fig. 4b) indicates around 12 dB to 15 dB improvement of contrast as compared with the original microbubble profile without signal enhancement (Fig. 4c). Notably, method 3 outperforms the other methods by providing the highest contrast improvement (14.8 dB, Fig. 4c). Note that for method 2 and 3, the similarity map is calculated from multiple consecutive ultrasound frames (50 frames in this study). Consequently, microbubble may traverse a certain distance within this multi-frame period, leading to blurring in the similarity map along the direction of microbubble motion (as exemplified by arrows in Fig. 3c).

B. *In vivo microbubble data of kidney transplant*

The acquired B-mode image of the kidney transplant is depicted in Fig. 5a, and the corresponding microbubble image obtained after tissue clutter filtering is presented in Fig. 5b (refer to a video of microbubble in supplemental video 2a). The similarity maps generated by four different methods for this microbubble image are illustrated in Fig. 5c. For method 1, each pixel of the similarity map is calculated from a spatial kernel and thus the spatial resolution of similarity map can be slightly compromised. Methods 2 and 3 incorporate multiple

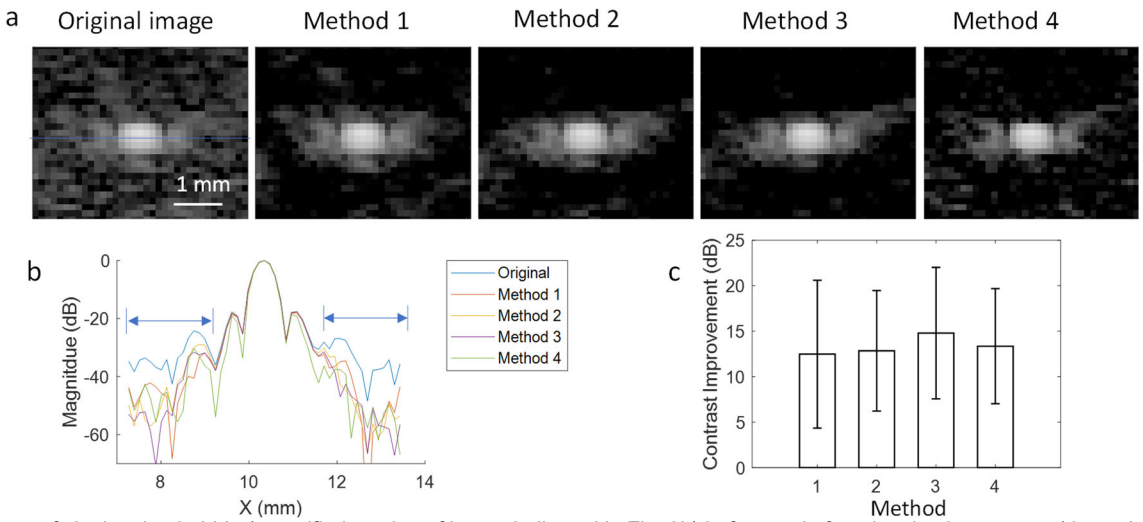

Fig. 4. (a) Image of single microbubble (magnified section of image indicated in Fig. 3b) before and after signal enhancement (dynamic range of [-50 0] dB). (b) Lateral profiles of the microbubble extracted from the blue line in Fig. 4a. (c) Contrast improvement relative to the original profile without signal enhancement, computed as the average of the profile segments of the background (indicated by the arrows in Fig. 4b).

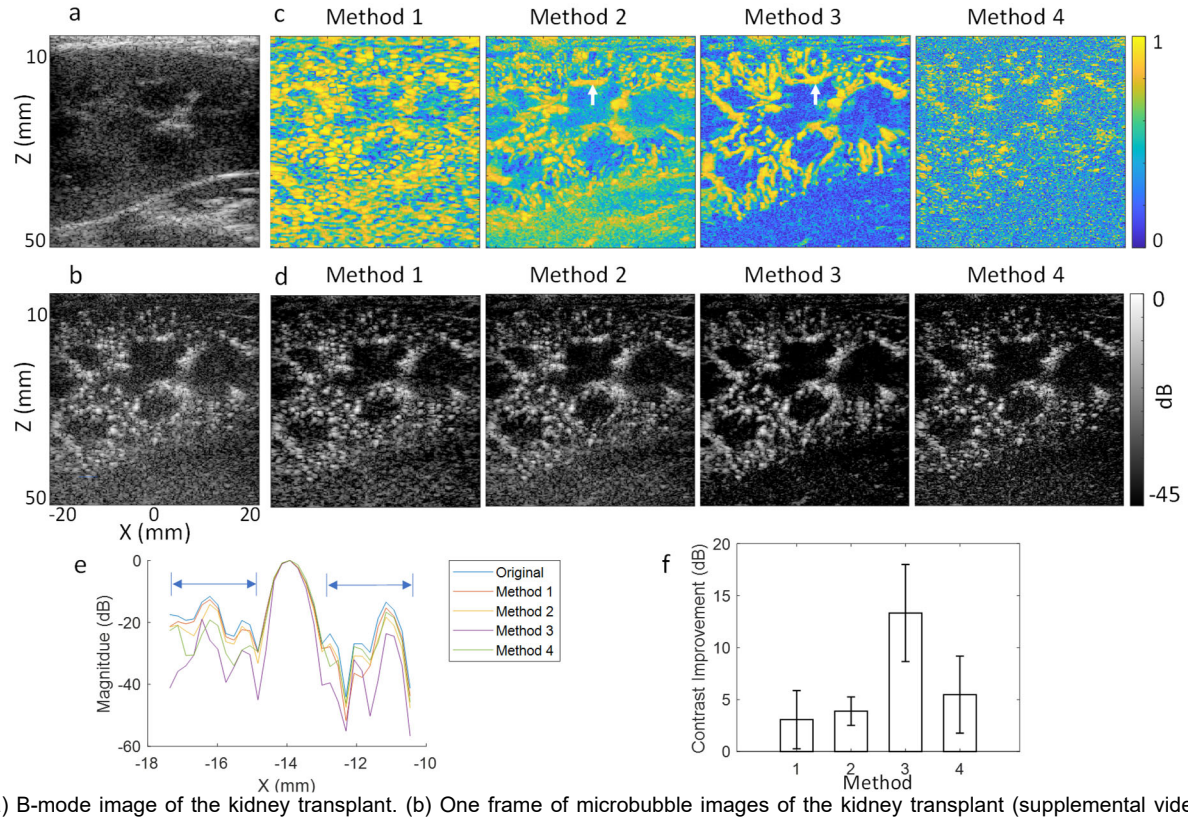

Fig. 5. (a) B-mode image of the kidney transplant. (b) One frame of microbubble images of the kidney transplant (supplemental video 2a). (c) Similarity maps for this microbubble image obtained using four different methods. (d) Corresponding enhanced microbubble images obtained from pixelwise weighting of the original microbubble image (Fig. 5b) using the similarity maps (supplemental videos 2b-2e). (e) Lateral profiles of one representative microbubble at a depth of ~ 45 mm, indicated by the blue line in Fig. 5b. (f) Contrast improvement, calculated as the average of the profile segments of the background (indicated by the arrows in Fig. 5e) as compared with the original microbubble profile without enhancement.

temporal ultrasound frames in similarity measurement, leading to visible microbubble moving trajectories in the resultant similarity maps (as indicated by the arrows in Fig. 5c). In method 4, the similarity map is solely estimated from the pre-compounded data used to perform spatial compounding of the given microbubble frame, and thus associated with highest temporal resolution of similarity measurement. Applying these similarity maps as weighting maps to the original microbubble image (Fig. 5b) results in improved contrast and visibility of the microbubble, as shown in Fig. 5d (see supplemental videos 2b-2e for a stack of images). For quantitative analysis, the profile of a representative microbubble at a depth of about 45 mm (indicated by the line in Fig. 5b) is presented in Fig. 5e. This microbubble demonstrates a contrast improvement (calculated as the average of the profile segments of the background indicated by the arrows in Fig. 5e) from about 3 dB to 13 dB, as compared with the original microbubble data without signal enhancement (Fig. 5f). Notably, method 1

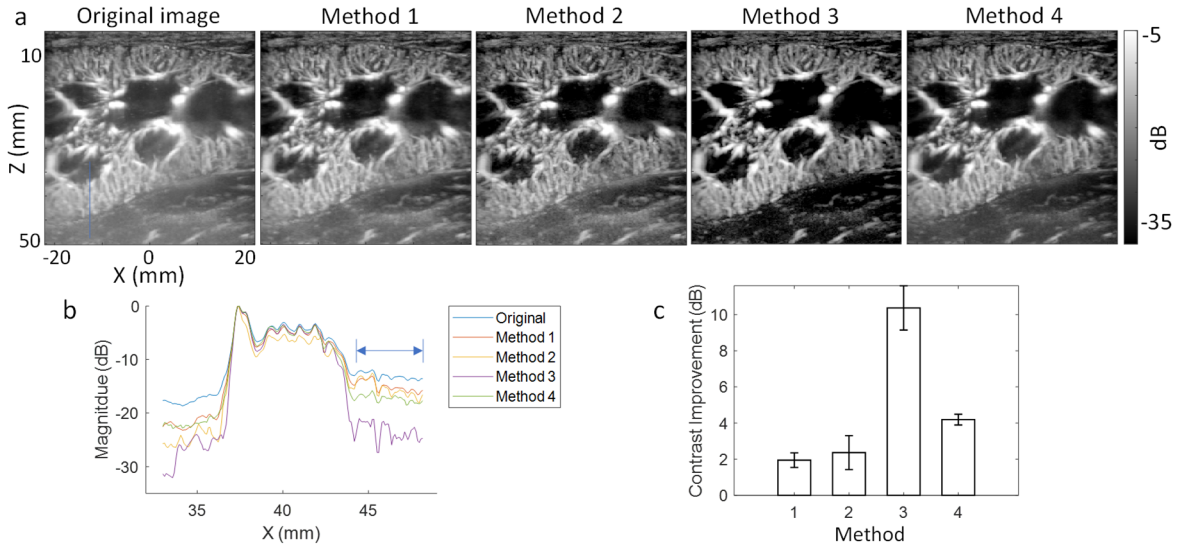

Fig. 6. (a) Microbubble-based power Doppler image of the kidney transplant obtained with or without signal enhancement. (b) Profiles of the power Doppler images around a depth of 40 mm indicated by the blue line in Fig.6a. The arrow indicates the profile segment of the background region, the average of which provides an estimate of (c) contrast improvement as compared with the original microbubble profile without enhancement.

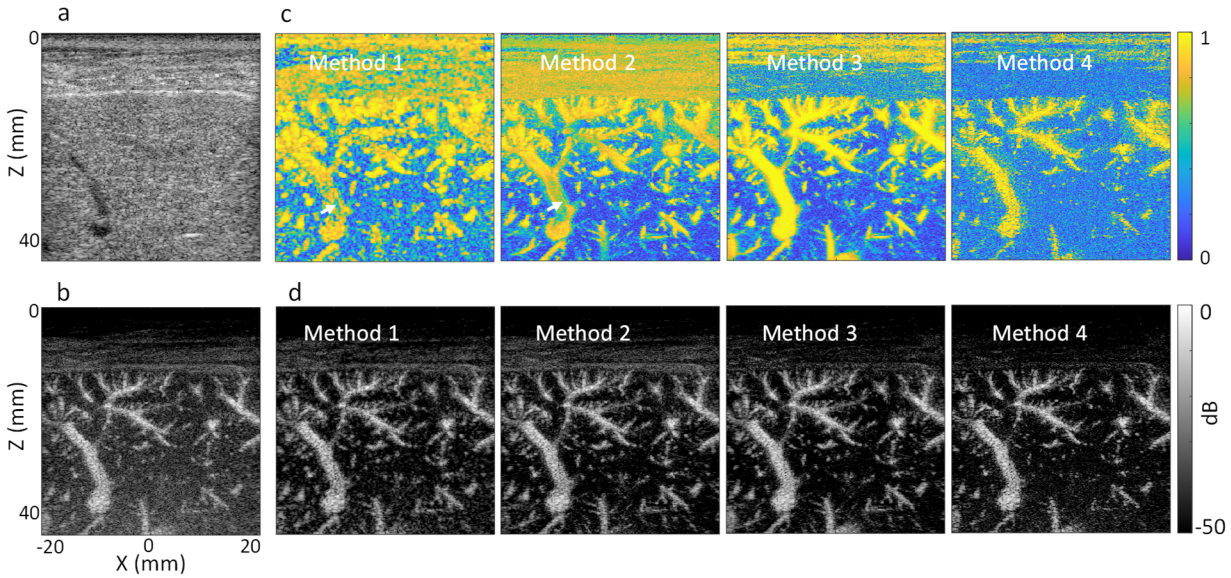

Fig. 7. (a) B-mode image of the human liver. (b) Representative microflow speckle image of the liver without using microbubbles (supplemental video 3a). (c) Similarity maps for this microflow speckle image obtained using four different methods. (d) Corresponding microflow speckle images after signal enhancement based on the similarity measurement (supplemental videos 3b-3e).

provides the least contrast improvement (3.1 dB), while method 3 yields the best microbubble contrast improvement (13.3 dB), consistent with the findings from the vessel phantom study.

In addition to improving the contrast of individual microbubble signals on a frame-by-frame basis, the proposed methods are also beneficial to the power Doppler image obtained by accumulating the power of enhanced microbubble signals along temporal dimension, as depicted in Fig. 6a. A profile of these microbubble-based power Doppler images around a depth of 40 mm (indicated by the blue line in Fig. 6a) is plotted for all the methods versus the original data without enhancement, as shown in Fig. 6b, revealing a consistent improvement of signal contrast compared to the background (from 1.9 dB to 10.4 dB, indicated in Fig. 6c). Again, method 3, which leverages the signal coherence of two subsets of data, attains the highest contrast gain in this context, consistent with the results for individual microbubble signal in Fig. 5.

C. *In vivo noncontrast blood flow data of liver*

Results of noncontrast blood flow imaging in a human liver are shown in Figs. 7 and 8. Unlike the spatially isolated microbubble signal, the backscattering echo signals of blood flow in the vasculature, obtained after tissue clutter filtering, exhibit a dominant speckle pattern (Fig. 7b). The changes in blood speckle patterns over time provide an alternative visual representation of flow dynamics in small vessels, as exemplified in supplemental video 3a. The similarity maps corresponding to this microflow speckle image (Fig. 7b) calculated using the four different methods are presented in Fig. 7c. In method 1, the spatial resolution of the similarity map is relatively lower compared to the other three methods, as the calculation involves a spatial kernel around each pixel (Fig. 7c). Additionally, speckle signals tend to de-correlate faster for flow in larger vessels, leading to reduced similarity levels at these

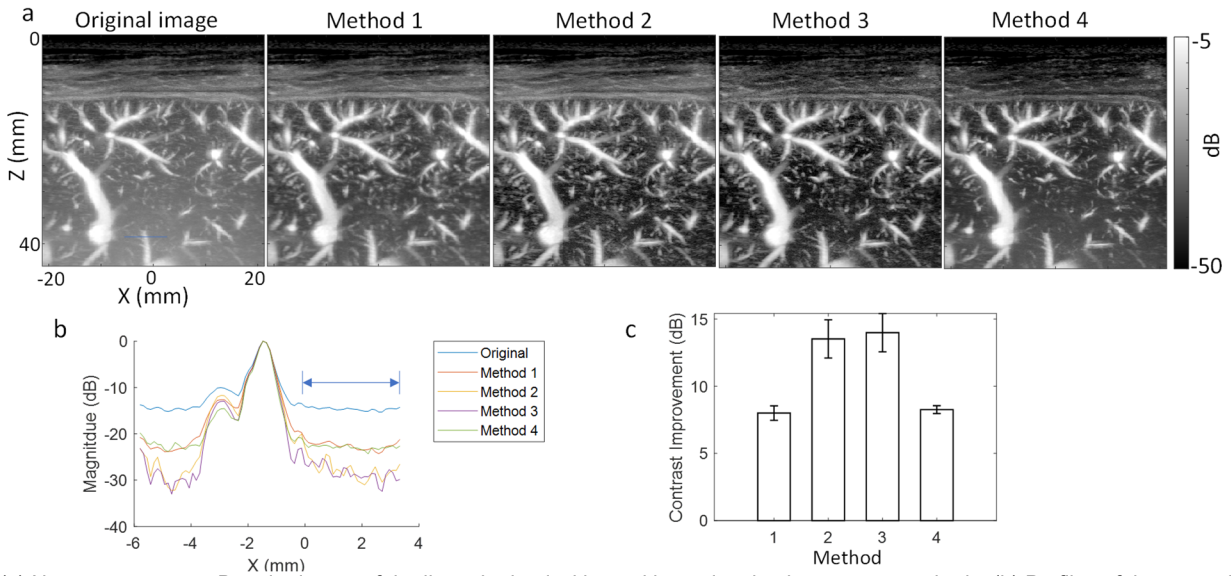

Fig. 8. (a) Noncontrast power Doppler image of the liver obtained with or without signal enhancement methods. (b) Profiles of the power Doppler images across a vessel at a depth of ~40 mm indicated by the blue line in Fig.8a. The arrow indicates the profile segment of the background region, the average of which provides an estimate of (c) contrast improvement as compared with the original vessel profile without enhancement.

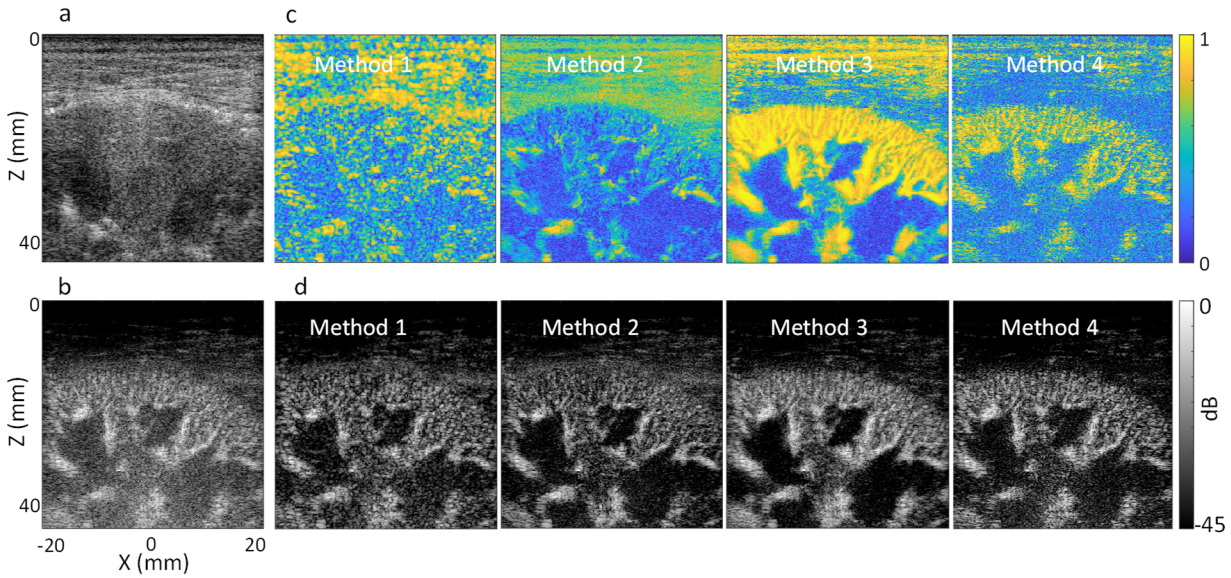

Fig. 9. (a) B-mode image of the human kidney. (b) Representative microflow speckle image of the kidney without using microbubbles (supplemental video 4a). (c) Similarity maps for this microflow speckle image obtained using four different methods. (d) Corresponding microflow speckle images after signal enhancement based on the similarity measurement (supplemental videos 4b-4e).

positions (indicated by the arrows in Fig. 7c) for methods 1 and 2. This effect is attributed to the relative low frame rate of the post-compounded data used in method 1 and 2, causing fast flow speckle to undergo significant changes between consecutive frames. In contrast, methods 3 and 4 better preserve signal coherence and provide improved similarity measurement in these scenarios, as they leverage the variation of flow signal two highly temporally overlapping subsets or across angular direction at a high PRF. Although retaining a high temporal resolution in similarity calculation, method 4 produces a visually noisier similarity map as compared to other methods. The enhanced microflow speckle images of the liver are presented in Fig. 7d (refer to supplemental videos 3b-3e), revealing improved blood flow contrast as compared with Fig. 7b. The enhancement is also reflected in the corresponding power Doppler images, as shown in Fig. 8a. The cross profile of a vessel at a depth of ~40 mm (indicated by the blue line in Fig. 8a) is plotted in Fig. 8b. The contrast improvement (computed as the average of the background profile segment) in relative to the original vessel profile without signal enhancement is shown to be ranging from 8.0 dB to 14.0 dB, as indicated in Fig. 8c. Similarly, method 3 outperforms the other methods in terms of contrast improvement (14.0 dB) in the current imaging settings.

D. *In vivo* noncontrast blood flow data of kidney

Kidney is a highly vascularized organ with high microvessel density and fast flow speed, leading to a faster de-correlation of blood flow signal and posing challenges for similarity measurement based on the post-compounding data with relatively low frame rate. Consequently, the similarity level is generally low in the kidney cortex and larger vessels regions for both methods 1 and 2, as indicated in Fig. 9c. Method 3, however, provides a robust similarity measurement for this complex flow application. Figure 9d shows the microflow speckle images of the kidney enhanced by the proposed methods, depicting improved contrast compared with the image before signal enhancement (Fig. 9b, see supplemental videos 4a-4e for dynamic microflow speckle images before and after signal enhancement). The corresponding microvessel power Doppler images of the kidney are shown in Fig. 10a, with the cross profiles of the power Doppler images at a depth of ~34 mm (indicated by the blue line in Fig. 10a) plotted in Fig. 10b. The contrast of power Doppler in relation to the background region (profile segment indicated by the arrow in Fig. 10b) indicates a range of 5.7dB to 16.3 dB improvement compared to the original image without signal enhancement (Fig. 10c). Among four methods, method 3 provides the most robust similarity measurements and thus achieves the highest gain in signal enhancement, consistent with results in above studies. Method 4 can preserve the similarity estimation for fast flow in kidney, but the noisy similarity map leads to only moderate gain in the signal contrast (Fig. 10c).

IV. Discussion

Enhancing the detection of microbubbles and blood flow, especially in challenging clinical imaging scenarios, is crucial for advancing ultrasound technologies like ULM and ultrafast ultrasound Doppler. In this study, we developed methods to enhance the contrast of microbubble and blood flow imaging by leveraging the unique spatial-temporal patterns exhibited by the microbubble/blood flow signals in comparison to background noise. Noise tends to exhibit high variability in pixel intensity/phase, while microbubble or blood flow signals demonstrate greater coherence between consecutive ultrasound frames. Through the quantification of signal similarity among ultrasound data, we effectively identified and enhanced target signals while suppressing noise. This involved incorporating the measured similarity levels back into the image using a pixelwise weighting process to improve signal contrast. We demonstrated the feasibility and efficacy of these methods in microbubble imaging through vessel phantom and *in vivo* kidney transplant studies. Furthermore, we applied these methods to microvascular imaging without using microbubble contrast agents and demonstrated their effectiveness in both human liver and kidney *in vivo*. Notably, the proposed methods

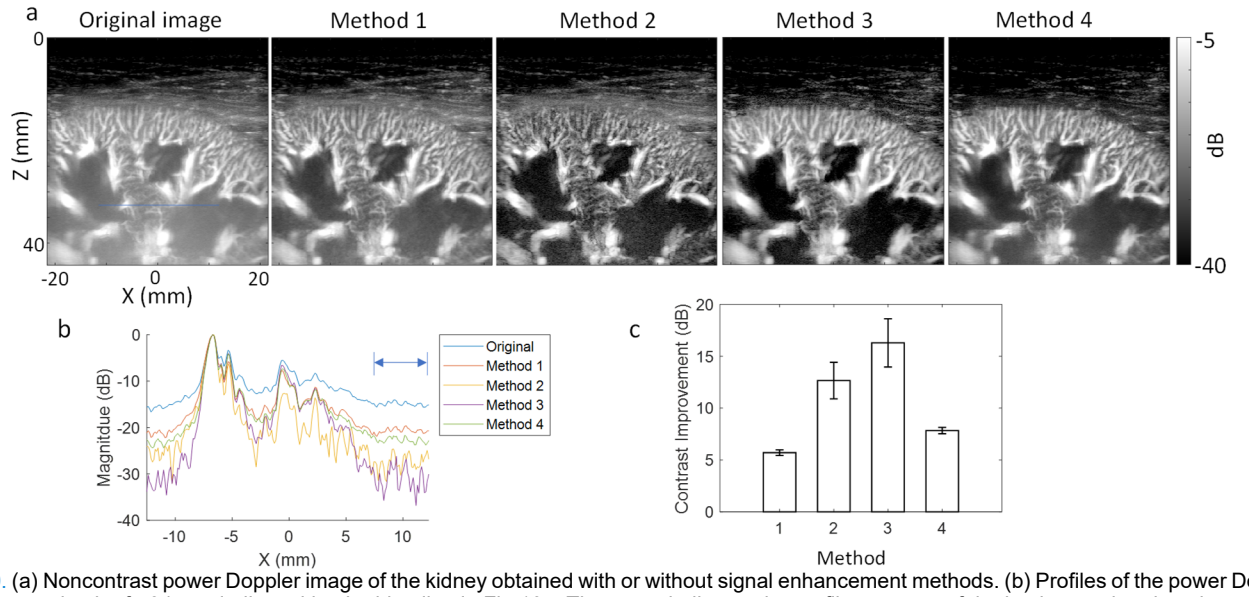

Fig. 10. (a) Noncontrast power Doppler image of the kidney obtained with or without signal enhancement methods. (b) Profiles of the power Doppler images at a depth of ~34 mm indicated by the blue line in Fig.10a. The arrow indicates the profile segment of the background region, the average of which provides an estimate of (c) contrast improvement as compared with the original vessel profile without enhancement.

are solely based on the beamformed data within the regular plane wave imaging framework, without requiring access to channel data or significant modification to the plane wave imaging sequence. This flexibility of the methods potentially allows for widespread integration into current ultrafast ultrasound imaging setups or retrospective analysis of existing plane wave imaging datasets. The robust and easy-to-implement nature of these methods holds promise for improved microbubble and microvascular imaging in future clinical translation.

The proposed similarity measurement methods leverage various aspects of signal coherence by flexibly handling beamformed plane wave data, either before or after spatial compounding. These methods mainly exploit the spatial (method 1), temporal (method 2), angular (method 4), or a combination (method 3) of signal characteristics, and their performance also differs slightly between microbubble imaging and noncontrast blood flow imaging. In the context of microbubble imaging, methods 1 and 2 provide less improvement of contrast than other methods. Nevertheless, these two methods handle the least amount of data in signal processing as only the post-compounded data is needed and can be readily extended to other high frame rate imaging dataset, such as the focused line-by-line Doppler imaging data commonly available in conventional clinical or preclinical scanners [40]. Among these two methods, method 1 calculates each pixel of the similarity map using a spatial block of data, thus compromising the spatial resolution of the resultant similarity measurement. In contrast, method 2 estimates signal coherence at a single pixel position across multiple ultrasound frames, providing better spatial resolution by scarifying the temporal resolution. Among the four methods, method 3 consistently yields the best contrast improvement. However, similar to method 2, its drawback is the requirement of using multiple temporal frames for the calculation of one similarity map. Microbubbles may traverse a certain distance during this multi-frame period, leading to microbubble trajectories observed in the resultant similarity map, potentially compromising spatial resolution in the microbubble moving direction. Method 4 has the highest temporal resolution in similarity calculation, as the similarity map of one compounded frame is solely calculated from the corresponding angular plane wave data of this frame. However, a significant drawback of this method is the computational cost associated with the SVD clutter filtering, which must be done for data of every transmitted angle separately. Additionally, a larger transmitting angle span may decrease the angular coherence [35], and therefore the maximum angle span should also be limited to maintain adequate angular coherence of the microbubble signal for the differentiation from noise. Moreover, the number of angles in plane wave imaging determines the number of samples (*i.e.*, the N_a in Eqn. 4) in the similarity calculation, which is typically limited in clinical applications and consequently associated with a noisier similarity estimate. This may be alleviated by increasing the number of transmitted angles, but at a cost of post-compounded frame rate. Therefore, there is certain tradeoff between contrast improvement, spatial resolution, temporal resolution, processing flexibility, and computational cost among methods for optimal microbubble detection performance.

In blood flow imaging without using microbubbles, the backscattering ultrasound speckles from the red blood cells are generally weaker and less coherent than that of the individual microbubble signals. The noncontrast liver and kidney results highlight significant decorrelation of flow speckle signals in methods 1 and 2 for fast flow, especially in larger vessels, necessitating a higher frame rate for improved similarity measurement based on compounded data. Although a slight contrast improvement can still be achieved, there may be undesired suppression of fast flow signals due to the reduced similarity level estimated from methods 1 and 2 with the current imaging setup. This may compromise the visualization of microvessel structures, particularly in scenarios with complex flow dynamics, such as imaging of the kidney cortex. In contrast, method 3 effectively preserves the correlation of flow speckle signals for improved similarity measurement and signal

enhancement even in highly complex flow scenarios. This is primarily attributed to the high coherence of the two data subsets used in cross-correlation calculation, as they are highly interleaved in both temporal and angular directions. Moreover, the drawback of method 3 in sparse microbubble imaging, *i.e.*, the presence of microbubble trajectories in the similarity map, is no longer exist in noncontrast blood flow speckle imaging. Therefore, given the current imaging setup, method 3 performs the best for noncontrast blood flow imaging, including both microflow speckle imaging and power Doppler imaging modes. Although method 4 can also preserve signal correlation well for fast flow by leveraging angular data at a high PRF, the similarity measurement is much noisier (Figs. 7 and 9) due to the lower SNR of the individual angular plane wave data and the limited number of transmitted angles that can be utilized. This issue is more significant for noncontrast imaging, as the flow signal is substantially weaker than the hyperechoic microbubble signal. Consequently, the performance of method 4 for noncontrast blood flow imaging seems to be less effective than for microbubble imaging. Therefore, method 3 is recommended for noncontrast imaging scenarios according to the findings of this study, which provides a good balance between computational cost and contrast improvement.

The concept of leveraging signal coherence among two beamformed data subsets like method 3 here to suppress noise and enhance signal detectability has been previously explored [19, 20]. However, previous methods typically employ nonnormalized cross-correlation coefficient of the subsets as an estimate of power Doppler with uncorrelated noise suppressed. In contrast, our study utilizes the normalized cross-correlation coefficient as a measurement of signal similarity, serving as an indicator of the likelihood of a pixel being a true target signal. This similarity measure is then employed as a weighting mask, applied to enhance pixels of target signal, and suppress pixels of noise on a frame-by-frame basis. This weighting strategy is advantageous for the detection of individual microbubble signals and the improvement of microflow speckle imaging, which are distinct from the previous methods that primarily focus on power Doppler images generated through the accumulation or correlation of a long packet of frames. Furthermore, the similarity-based weighting methods presented here can also be readily applied to further improve power Doppler images in conjunction with these existing methods. For instance, we previously presented a method that calculate the nonnormalized cross-correlation of the two data subsets as the final blood flow image with noise suppressed [20]. Figure 11a shows an example of this cross-correlation based blood flow image using the same noncontrast liver data (data subsets generated Fig. 1e), which indicates an improved performance compared to the original power Doppler image (Fig. 8a). A similarity map can be generated at the same time using these two subsets following method 3, which can be used to further boost the contrast of this blood flow image, as the example shown in Fig. 11b.

The underlying principle of these weighting-based methods is to identify pixels of target signal based on their similarity levels and apply higher weights to these pixels to achieve signal enhancement in comparison to the noisy background. However, at each individual pixel, the ratio of noise and signal components remain unchanged, and thus, the SNR of this pixel has not been modified, which represents the major limitation of these kinds of weighting-based methods. Despite this limitation, the methods prove advantageous for enhancing the signal contrast in comparison to the noise-dominant background regions in the applications of microbubble and blood flow imaging. The concept of similarity measurement and weighting process may also be extended to specific applications of soft tissue imaging (like B-mode), to enhance tissue contrast in relation to neighboring hypoechoic regions like vessel lumen, bladder, and heart chambers. Exploring these applications, however, is beyond the scope of the current study. For quantitative evaluation of different methods proposed in this study, we opted to plot a representative signal profile and calculate the contrast of the target signal versus the neighborhood background area. While this approach may not represent situation at all spatial positions, it meets the purpose of demonstrating improvement and making comparisons among the four methods. It is acknowledged that there are many other methods of choice for similarity measure, while our study specifically focuses on correlation-based analysis. Whether other similarity or coherence analyses might offer better performance remains open for future investigation. Nevertheless, the conceptual framework of similarity-based microbubble and blood flow signal enhancement is easily adaptable from 2D to 3D imaging, thereby broadening its applicability.

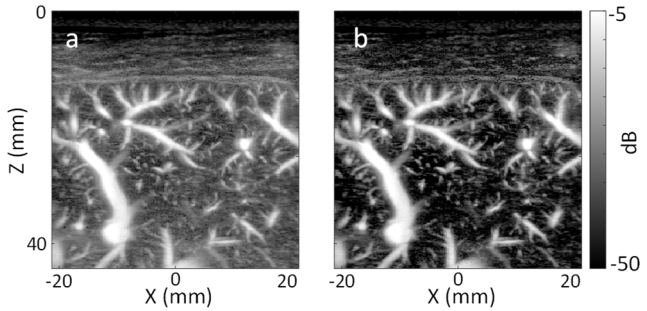

Fig. 11. (a) Ultrasound vascular imaging of the liver by the method presented in [20], and (b) the combination of this method with the similarity-based method presented in this study to further enhance the image contrast.

V. Conclusion

In summary, we have proposed several methods designed to enhance signal contrast in ultrasound microbubble and blood flow imaging by leveraging the spatial-temporal coherence of the beamformed ultrasound data within the plane wave imaging framework. We demonstrated the feasibility of these methods in phantom and *in vivo* studies for applications with and without using microbubble contrast agents. The robust and easy-to-implement nature of these methods hold promise for improved microbubble detection and microvascular imaging for widespread clinical translation.

References

[1] D. H. Evans, J. A. Jensen, and M. B. Nielsen, "Ultrasonic colour Doppler imaging," *Interface Focus,* vol. 1, no. 4, pp. 490-502, Aug 6 2011.

[2] M. X. Tang *et al.*, "Quantitative contrast-enhanced ultrasound imaging: a review of sources of variability," *Interface Focus,* vol. 1, no. 4, pp. 520-539, Aug 2011.

[3] C. F. Dietrich *et al.*, "How to perform Contrast-Enhanced Ultrasound (CEUS)," *Ultrasound Int Open,* vol. 4, no. 1, pp. E2-e15, Jan 2018.

[4] O. Couture, S. Bannouf, G. Montaldo, J. F. Aubry, M. Fink, and M. Tanter, "Ultrafast imaging of ultrasound contrast agents," *Ultrasound Med Biol,* vol. 35, no. 11, pp. 1908-16, Nov 2009.

[5] O. Couture, V. Hingot, B. Heiles, P. Muleki-Seya, and M. Tanter, "Ultrasound Localization Microscopy and Super-Resolution: A State of the Art," *IEEE Trans. Ultrason. Ferroelectr. Freq. Control,* vol. 65, no. 8, pp. 1304-1320, Aug 2018.

[6] C. Errico *et al.*, "Ultrafast ultrasound localization microscopy for deep super-resolution vascular imaging," *Nature,* vol. 527, no. 7579, pp. 499-+, Nov 2015.

[7] K. Christensen-Jeffries *et al.*, "Super-Resolution Ultrasound Imaging," *Ultrasound Med. Biol.,* vol. 46, no. 4, pp. 865-891, Apr 2020.

[8] E. Mace, G. Montaldo, B. F. Osmanski, I. Cohen, M. Fink, and M. Tanter, "Functional Ultrasound Imaging of the Brain: Theory and Basic Principles," *IEEE Trans. Ultrason. Ferroelectr. Freq. Control,* vol. 60, no. 3, pp. 492-506, Mar 2013.

[9] A. C. H. Yu and L. Lovstakken, "Eigen-Based Clutter Filter Design for Ultrasound Color Flow Imaging: A Review," *IEEE Trans. Ultrason. Ferroelectr. Freq. Control,* vol. 57, no. 5, pp. 1096-1111, May 2010.

[10] C. Demene *et al.*, "Spatiotemporal Clutter Filtering of Ultrafast Ultrasound Data Highly Increases Doppler and fUltrasound Sensitivity," *IEEE Trans. Med. Imaging,* vol. 34, no. 11, pp. 2271-2285, Nov 2015.

[11] J. Bercoff *et al.*, "Ultrafast Compound Doppler Imaging: Providing Full Blood Flow Characterization," *IEEE Trans. Ultrason. Ferroelectr. Freq. Control,* vol. 58, no. 1, pp. 134-147, Jan 2011.

[12] R. Y. Chiao, L. Y. Mo, A. L. Hall, S. C. Miller, and K. E. Thomenius, "B-mode blood flow (B-flow) imaging," in *2000 IEEE Ultrasonics Symposium. Proceedings. An International Symposium (Cat. No.00CH37121)*, 2000, vol. 2, pp. 1469-1472 vol.2.

[13] L. Løvstakken, S. Bjaerum, D. Martens, and H. Torp, "Blood flow imaging--A new real-time, 2-D flow imaging technique," *IEEE Trans Ultrason Ferroelectr Freq Control,* vol. 53, no. 2, pp. 289-99, Feb 2006.

[14] B. Y. Yiu and A. C. Yu, "High-frame-rate ultrasound color-encoded speckle imaging of complex flow dynamics," *Ultrasound Med Biol,* vol. 39, no. 6, pp. 1015-25, Jun 2013.

[15] C. Tremblay-Darveau *et al.*, "Improved Contrast-Enhanced Power Doppler Using a Coherence-Based Estimator," *IEEE Trans. Med. Imaging,* vol. 36, no. 9, pp. 1901-1911, Sep 2017.

[16] A. Bar-Zion, C. Tremblay-Darveau, O. Solomon, D. Adam, and Y. C. Eldar, "Fast Vascular Ultrasound Imaging With Enhanced Spatial Resolution and Background Rejection," *IEEE Trans. Med. Imaging,* vol. 36, no. 1, pp. 169-180, Jan 2017.

[17] J. Kang, D. Go, I. Song, and Y. Yoo, "Ultrafast Power Doppler Imaging Using Frame-Multiply-and-Sum-Based Nonlinear Compounding," *IEEE Transactions on Ultrasonics, Ferroelectrics, and Frequency Control,* vol. 68, no. 3, pp. 453-464, 2021.

[18] C. C. Shen and Y. C. Chu, "DMAS Beamforming with Complementary Subset Transmit for Ultrasound Coherence-Based Power Doppler Detection in Multi-Angle Plane-Wave Imaging," *Sensors (Basel),* vol. 21, no. 14, Jul 16 2021.

[19] A. Stanziola, C. H. Leow, E. Bazigou, P. D. Weinberg, and M.-X. Tang, "ASAP: Super-Contrast Vasculature Imaging using Coherence Analysis and High Frame- Rate Contrast Enhanced Ultrasound," *IEEE Transactions on Medical Imaging* vol. PP, no. 99, pp. 1-1, Feb 2018.

[20] C. Huang *et al.*, "Simultaneous Noise Suppression and Incoherent Artifact Reduction in Ultrafast Ultrasound Vascular Imaging," *IEEE Trans Ultrason Ferroelectr Freq Control,* vol. 68, no. 6, pp. 2075-2085, Jun 2021.

[21] C. Huang, P. Song, P. Gong, J. D. Trzasko, A. Manduca, and S. Chen, "Debiasing-Based Noise Suppression for Ultrafast Ultrasound Microvessel Imaging," *IEEE Transactions on Ultrasonics, Ferroelectrics, and Frequency Control,* vol. 66, no. 8, pp. 1281-1291, 2019.

[22] R. Nayak, M. Fatemi, and A. Alizad, "Adaptive background noise bias suppression in contrast-free ultrasound microvascular imaging," *Physics in Medicine & Biology,* vol. 64, no. 24, p. 245015, 2019/12/19 2019.

[23] P. F. Song, A. Manduca, J. D. Trzasko, and S. G. Chen, "Noise Equalization for Ultrafast Plane Wave Microvessel Imaging," *IEEE Trans. Ultrason. Ferroelectr. Freq. Control,* vol. 64, no. 11, pp. 1776-1781, Nov 2017.

[24] J. Brown *et al.*, "Investigation of Microbubble Detection Methods for Super-Resolution Imaging of Microvasculature," *IEEE Trans Ultrason Ferroelectr Freq Control,* vol. 66, no. 4, pp. 676-691, Apr 2019.

[25] K. G. Brown and K. Hoyt, "Evaluation of Nonlinear Contrast Pulse Sequencing for Use in Super-Resolution Ultrasound Imaging," *IEEE Trans Ultrason Ferroelectr Freq Control,* vol. 68, no. 11, pp. 3347-3361, Nov 2021.

[26] E. P. Vienneau and B. C. Byram, "A Coded Excitation Framework for High SNR Transcranial Ultrasound Imaging," *IEEE Trans Med Imaging,* vol. 42, no. 10, pp. 2886-2898, Oct 2023.

[27] J. Baranger, B. Arnal, F. Perren, O. Baud, M. Tanter, and C. Demene, "Adaptive spatiotemporal SVD clutter filtering for Ultrafast Doppler Imaging using similarity of spatial singular vectors," *IEEE Trans. Med. Imaging,* vol. PP, no. 99, pp. 1-1, Feb 2018.

[28] P. F. Song, A. Manduca, J. D. Trzasko, and S. G. Chen, "Ultrasound Small Vessel Imaging With Block-Wise Adaptive Local Clutter Filtering," *IEEE Trans. Med. Imaging,* vol. 36, no. 1, pp. 251-262, Jan 2017.

[29] M. Kim, Y. Zhu, J. Hedhli, L. W. Dobrucki, and M. F. Insana, "Multidimensional Clutter Filter Optimization for Ultrasonic Perfusion Imaging," *IEEE Trans. Ultrason. Ferroelectr. Freq. Control,* vol. 65, no. 11, pp. 2020-2029, Nov 2018.

[30] K. A. Ozgun and B. C. Byram, "Multidimensional Clutter Filtering of Aperture Domain Data for Improved Blood Flow Sensitivity," *IEEE Trans Ultrason Ferroelectr Freq Control,* vol. 68, no. 8, pp. 2645-2656, Aug 2021.

[31] Y. Sui *et al.*, "Randomized Spatial Downsampling-Based Cauchy-RPCA Clutter Filtering for High-Resolution Ultrafast Ultrasound Microvasculature Imaging and Functional Imaging," *IEEE Trans Ultrason Ferroelectr Freq Control,* vol. 69, no. 8, pp. 2425-2436, Aug 2022.

[32] R. R. Wildeboer *et al.*, "Blind Source Separation for Clutter and Noise Suppression in Ultrasound Imaging: Review for Different Applications," *IEEE Transactions on Ultrasonics, Ferroelectrics, and Frequency Control,* vol. 67, no. 8, pp. 1497-1512, 2020.

[33] Y. L. Li and J. J. Dahl, "Coherent Flow Power Doppler (CFPD): Flow Detection Using Spatial Coherence Beamforming," *IEEE Trans. Ultrason. Ferroelectr. Freq. Control,* vol. 62, no. 6, pp. 1022-1035, Jun 2015.

[34] Y. L. Li, D. Hyun, L. Abou-Elkacem, J. K. Willmann, and J. J. Dahl, "Visualization of Small-Diameter Vessels by Reduction of Incoherent Reverberation With Coherent Flow Power Doppler," *IEEE Trans. Ultrason. Ferroelectr. Freq. Control,* vol. 63, no. 11, pp. 1878-1889, Nov 2016.

[35] Y. L. Li and J. J. Dahl, "Angular coherence in ultrasound imaging: Theory and applications," *J. Acoust. Soc. Am.,* vol. 141, no. 3, pp. 1582-1594, Mar 2017.

[36] M. Jakovljevic *et al.*, "Blood Flow Imaging in the Neonatal Brain Using Angular Coherence Power Doppler," *IEEE Trans Ultrason Ferroelectr Freq Control,* vol. 68, no. 1, pp. 92-106, Jan 2021.

[37] L. Huang *et al.*, "High-Quality Ultrafast Power Doppler Imaging Based on Spatial Angular Coherence Factor," *IEEE Trans Ultrason Ferroelectr Freq Control,* vol. 70, no. 5, pp. 378-392, May 2023.

[38] B. Pialot *et al.*, "Adaptive noise reduction for power Doppler imaging using SVD filtering in the channel domain and coherence weighting of pixels," *Phys Med Biol,* vol. 68, no. 2, Jan 2 2023.

[39] J. M. Rubin *et al.*, "Fractional moving blood volume: estimation with power Doppler US," *Radiology,* vol. 197, no. 1, pp. 183-190, 1995.

[40] C. Huang *et al.*, "Noninvasive Contrast-Free 3D Evaluation of Tumor Angiogenesis with Ultrasensitive Ultrasound Microvessel Imaging," *Sci Rep,* vol. 9, no. 1, p. 4907, 2019/03/20 2019.